Clim. Past, 19, 2445–2462, 2023
https://doi.org/10.5194/cp-19-2445-2023
© Author(s) 2023. This work is distributed under
the Creative Commons Attribution 4.0 License.

Climate of the Past
Open Access

Simulating dust emissions and secondary organic aerosol formation over northern Africa during the mid-Holocene Green Sahara period

Putian Zhou[1], Zhengyao Lu[2], Jukka-Pekka Keskinen[3], Qiong Zhang[4], Juha Lento[5], Jianpu Bian[1], Twan van Noije[6], Philippe Le Sager[6], Veli-Matti Kerminen[1], Markku Kulmala[1], Michael Boy[1,7], and Risto Makkonen[1,3]

[1]Institute for Atmospheric and Earth System Research/Physics, Faculty of Science, University of Helsinki, Helsinki, Finland
[2]Department of Physical Geography and Ecosystem Science, Lund University, Lund, Sweden
[3]Finnish Meteorological Institute, 00560 Helsinki, Finland
[4]Department of Physical Geography and Bolin Centre for Climate Research, Stockholm University, Stockholm, Sweden
[5]CSC – IT Center for Science, Espoo, Finland
[6]Royal Netherlands Meteorological Institute (KNMI), De Bilt, the Netherlands
[7]School of Engineering Sciences, Lappeenranta-Lahti University of Technology LUT, Lahti, Finland

Correspondence: Putian Zhou (putian.zhou@helsinki.fi) and Risto Makkonen (risto.makkonen@fmi.fi)

Received: 6 July 2023 – Discussion started: 14 July 2023
Revised: 6 October 2023 – Accepted: 14 October 2023 – Published: 5 December 2023

Abstract. Paleo-proxy data indicate that a "Green Sahara" thrived in northern Africa during the early- to mid-Holocene (MH; 11 000 to 5000 years before present), characterized by more vegetation cover and reduced dust emissions. Utilizing a state-of-the-art atmospheric chemical transport model, TM5-MP, we assessed the changes in biogenic volatile organic compound (BVOC) emissions, dust emissions and secondary organic aerosol (SOA) concentrations in northern Africa during this period relative to the pre-industrial (PI) period. Our simulations show that dust emissions reduced from 280.6 Tg a^{-1} in the PI to 26.8 Tg a^{-1} in the MH, agreeing with indications from eight marine sediment records in the Atlantic Ocean. The northward expansion in northern Africa resulted in an increase in annual emissions of isoprene and monoterpenes during the MH, around 4.3 and 3.5 times higher than that in the PI period, respectively, causing a 1.9-times increase in the SOA surface concentration. Concurrently, enhanced BVOC emissions consumed more hydroxyl radical (OH), resulting in less sulfate formation. This effect counteracted the enhanced SOA surface concentration, altogether leading to a 17 % increase in the cloud condensation nuclei at 0.2 % super saturation over northern Africa. Our simulations provide consistent emission datasets of BVOCs, dust and the SOA formation aligned with the northward shift of vegetation during the "Green Sahara" period, which could serve as a benchmark for MH aerosol input in future Earth system model simulation experiments.

1 Introduction

A Green Sahara, instead of present desert Sahara, existed in northern Africa during the early- to mid-Holocene (MH) from 11 to 5 ka (11 000 to 5000 years before present: 1950), which is usually referred to as the African Humid Period (AHP, Claussen et al., 2017). Fossil pollen records suggest that tropical plants expanded northward up to 23° N (Hély et al., 2014), indicating a shift in vegetation patterns. Leaf wax analysis reveals a striking increase in annual precipitation in the western Sahara, from the present-day range of 35 to 100 mm to a substantial 640 mm during the AHP (Tierney et al., 2017). Paleo-hydrological records also depict a landscape dotted with lakes across northern Africa, extending at least to 28° N as shown by Lézine et al. (2011). These findings collectively paint a vivid picture of a once green and flourishing Sahara.

The higher summer insolation in the Northern Hemisphere due to Earth's orbital variation is considered to intensify the

West African Monsoon (WAM), leading to increased rainfall across northern Africa (Kutzbach, 1981). However, this theory is insufficient to explain the substantial rise in rainfall needed to maintain the vegetation cover over northern Africa, as shown in model simulations (Joussaume et al., 1999). The northward vegetation shift is correlated with a reduction in airborne mineral dust, suggesting that land cover change could contribute to the stronger WAM and enhanced rainfall. Pausata et al. (2016) demonstrated that considering reduced atmospheric dust levels could potentially push the WAM an additional 500 km northward under identical vegetation change. Egerer et al. (2018) showed improved rainfall modeling over northern Africa when introducing dynamic vegetation and interactive dust, compared to CMIP5 model results. Nevertheless, including the indirect effects of dust aerosol on stratiform rainfall could reduce dust-induced Saharan precipitation anomaly by about 13 % (Thompson et al., 2019). In addition, the larger lake and wetland extents over northern Africa during the MH could have also enhanced the WAM and precipitation as demonstrated in previous studies (e.g., Krinner et al., 2012; Specht et al., 2022). When including the feedbacks from vegetation, soil and surface lakes in the model simulations for the MH, Chandan and Peltier (2020) demonstrated that the modeled precipitation enhancement was sufficient to maintain the extended vegetation cover over the Sahel and Sahara regions, even without changing dust forces. Other hypotheses have also been proposed. For example, Menviel et al. (2021) suggested that the abrupt onset of AHP was mainly due to the strengthening of Atlantic Meridional Overturning Circulation (AMOC).

Vegetation, beyond altering the surface albedo and dust emissions, emits large quantities of biogenic volatile organic compounds (BVOCs) (Guenther et al., 2006, 2012). These BVOCs play a key role in biosphere–atmosphere interactions, they can be oxidized to low-volatile compounds to form secondary organic aerosol (SOA). SOA then modulates radiative forcing directly by scattering or absorbing shortwave radiation and indirectly by acting as cloud condensation nuclei (CCN) (Shrivastava et al., 2017). In the context of a Green Sahara, reduced dust emissions could have enhanced SOA formation efficiently due to lower condensation sinks and simultaneously have reduced the giant CCN concentration impeding the initiation of precipitation (Carslaw et al., 2010). Therefore, developing a comprehensive dataset of BVOC emissions, dust emissions and SOA concentration that is consistent with the reconstructed vegetation cover is important to understand northern Africa's climate change during the MH.

To date, this area has been relatively unexplored. Adams et al. (2001) estimated the global BVOC emissions based on reconstructed vegetation biome distribution at 8 and 5 ka. Furthermore, BVOCs produce new aerosol particles and due to their subsequent growth enhance CCN concentrations (Kulmala et al., 2004, 2014). Kaplan et al. (2006) examined BVOC impacts on MH methane concentration using a global vegetation model but failed to reproduce the northward vegetation shift over the Sahara. Therefore, in this study we aim to use state-of-the-art atmospheric chemical transport model simulations to provide the most comprehensive datasets of BVOC emissions, dust emissions and SOA concentrations in northern Africa, based on the consistently accurate vegetation simulation result from Lu et al. (2018). We also examined the consequential climate-relevant changes in aerosol optical properties and CCN to reveal their driving factors.

This study is organized as follows. In Sect. 2, the model TM5-MP is introduced and the detailed model configurations are described. This section also includes the description of the datasets of BVOC emissions from various sources, as well as how the reconstructed dust mass deposition flux data at different marine sediment locations are obtained. In Sect. 3, several aerosol-related quantities over Africa, especially northern Africa, during PI and MH periods are analyzed, e.g., the BVOC emissions, dust emissions and deposition fluxes, the surface concentrations of SOA and CCN and aerosol optical depth at 550 nm. The results are concluded in Sect. 4.

2 Methods and data

2.1 TM5-MP

The global chemical transport model TM5-MP (Tracer Model 5, Massively Parallel version; Krol et al., 2005; Huijnen et al., 2010; van Noije et al., 2014, 2021; Williams et al., 2017) has been applied in this study. It is driven by the input meteorological fields which are produced from ERA-Interim reanalysis datasets provided by the ECMWF (European Centre for Medium-range Weather Forecasts; Dee et al., 2011). The model accounts for gas-phase, aqueous-phase and heterogeneous chemistry. The gas-phase chemistry scheme is a modified version of the CB05 carbon bond mechanism (Yarwood et al., 2005), which was described in detail in Williams et al. (2017).

TM5-MP predicts aerosol dynamic processes using the two-moment modal model M7 (Vignati et al., 2004), which includes seven log-normally distributed modes with four water-soluble modes (nucleation, Aitken, accumulation and coarse) and three insoluble modes (Aitken, accumulation and coarse). Each mode corresponds to a specific dry diameter range: nucleation mode is less than 10 nm, Aitken mode ranges from 10 to 100 nm, accumulation mode from 100 nm to 1 µm and coarse mode is greater than 1 µm.

The current version of TM5-MP incorporates SOA into four soluble modes and the insoluble Aitken mode, resulting in a comprehensive aerosol model including SOA, sulfate, ammonium, nitrate, methane sulfonic acid (MSA), primary organic aerosol, black carbon, sea salt and mineral dust (Bergman et al., 2022). Isoprene and monoterpenes, acting as gaseous precursors of SOA, are from natural emissions calculated by MEGANv2.1 (Model of Emissions of Gases

and Aerosols from Nature version 2.1; Guenther et al., 2012; Sindelarova et al., 2014) and biomass burning emissions based on van Marle et al. (2017). The isoprene and monoterpenes can be oxidized by OH and O_3 in the air to form extremely low-volatility organic compounds (ELVOCs) and semi-volatile organic compounds (SVOCs). The ELVOCs first participate in new particle formation and the rest condense onto existing aerosol particles. The SVOCs only condense due to their higher volatilities. The particle formation and condensation processes occur within one time step, so the transport of ELVOCs and SVOCs is not simulated. More details are described in Bergman et al. (2022).

The dust emissions are calculated online based on the method introduced in Tegen et al. (2002) and extended by Heinhold et al. (2007). New dust emission parameterization methods have also been developed (e.g., Leung et al., 2023) but have not been implemented into the current TM5-MP version. Only the features related to this study are described here. Firstly, we proportion dust emissions to the non-vegetated area within a grid cell, which is determined by the vegetation cover data (see Eq. 1 in Tegen et al., 2002). When dominated by shrubs, we apply the maximum annual vegetation cover, whereas when grass dominates, we use the monthly value. Secondly, Tegen et al. (2002) simulated the potential maximum extent of lakes, and determined preferential dust source regions from the difference between the maximum areas and actual present-day lakes. These regions are assumed to contain silt aggregates composed of finer particles with a median particle radius of 15 µm in the Northern Hemisphere (NH) and 27 µm in the Southern Hemisphere (SH), requiring a smaller wind stress threshold to lift, which is 30 and 20 $cm\,s^{-1}$ in the NH and SH, respectively. Moreover, the ratio between the vertical dust flux and horizontal soil particle flux is also assumed to be the largest among all regions, which is set to $10^{-5}\,cm^{-1}$. All these factors have determined high dust emission fluxes over the preferential source regions. However, we should note that in TM5-MP, the threshold wind stress (u_{min}) is set to 13.75 $cm\,s^{-1}$ for all kinds of land covers, which reduce further when the cultivation cover exceeds 8% and the grid cell is dominated by either grass or shrub. For more details, see Tegen et al. (2002) and van Noije et al. (2021).

2.2 Model setup

Simulations have been conducted for five different cases: a PI control run (pi_ctrl), a PI run with the default TM5-MP configuration (pi_orig), a PI control run excluding anthropogenic emissions (pi_zero), a standard MH run (mh) and an MH run incorporating a Green Sahara and reduced dust (mh_gsrd) (Table 1). The model configuration for each case will be detailed subsequently. All simulations applied a horizontal resolution of 3° in longitude and 2° in latitude with 34 vertical hybrid-sigma levels. The base time step was set to 1 h. Each simulation ran for 2 years, with the first year serving as the spin-up and the results being analyzed from the second year. The 1-year spin-up in TM5-MP simulations was also applied in previous studies (e.g., Williams et al., 2017; Myriokefalitakis et al., 2020) and was validated here in a 12-year simulation test case (see Fig. S1 in the Supplement).

In all five simulation cases, the input meteorological data for spin-up simulations were derived from the year 2008, and the year 2009 was used for subsequent-year simulations, facilitating a focus on comparisons between individual cases. The vegetation cover data for pi_ctrl, mh and mh_gsrd cases were derived from respective PI, MH and MH_gsrd simulation results in Lu et al. (2018).

The anthropogenic emissions are set to 1850 levels for pi_orig and pi_ctrl cases and are switched off for mh and mh_gsrd cases. The natural emissions in 2009 are applied in pi_ctrl, pi_orig, mh and mh_gsrd cases, except that the emissions of isoprene and monoterpenes in pi_ctrl, mh and mh_gsrd cases are derived from the LPJ-GUESS (Lund-Potsdam-Jena General Ecosystem Simulator; Smith et al., 2001, 2014) simulation results of the PI, MH and MH_gsrd cases in Lu et al. (2018), respectively. Given that the simulation results from Lu et al. (2018) contained 10-year of equilibrium-state data, we applied the 10-year mean for both the vegetation and BVOC emission data (see Supplement). In mh and mh_gsrd cases, the mixing ratios of greenhouse gases CH_4 and CO_2 were set to 597.0 ppbv and 264.4 ppmv, respectively, according to the PMIP4-CMIP6 protocol for MH experiments (Otto-Bliesner et al., 2017). The configuration of natural emissions of isoprene and monoterpenes and the vegetation cover data in pi_ctrl, mh and mh_gsrd cases were applied globally.

The parameters used to calculate the dust emissions in pi_ctrl, mh and mh_gsrd cases are modified according to their input vegetation data and specific time period assumptions. Firstly, all preferential dust emission source areas, namely potential lake areas, within the region of northern Africa (20° W to 40° E and 10 to 30° N) are switched off in the mh and mh_gsrd cases, since we assume that these areas were actual lakes during MH period. A similar assumption was also applied in Egerer et al. (2018). Secondly, the land–sea mask ratio over these areas has also been set to zero, representing lake surface within these grids. Thirdly, the cultivation cover was set to zero for the mh and mh_gsrd cases, and for comparison, we made the same settings for the pi_ctrl case. Fourthly, within the TM5-MP model, vegetation cover impacting the dust emission fluxes is indirectly represented by FPAR (the fraction of absorbed photosynthetically active radiation) according to Tegen et al. (2002). Here we applied the monthly vegetation cover directly from LPJ-GUESS output data within the northern Africa region, and set the corresponding values to the FPAR variable for pi_ctrl, mh and mh_gsrd cases. The pi_orig applied the original model setup for the PI but with present-day meteorological input

Table 1. Model configurations of the simulation cases pi_ctrl, pi_orig, pi_zero, mh and mh_gsrd. The number 1850 and 2009 show the years that the input data are from. Here lsm means land–sea mask, PD is present-day lsm and MH is mid-Holocene lsm with paleo-lakes switched on as water surface. For vegetation, pi_mean, mh_mean and mh_gsrd_mean represent the 10-year mean of the simulation data from PI, MH and MH_gsrd cases in Lu et al. (2018), respectively. For the emissions of isoprene and monoterpenes, as well as the fraction of absorbed photosynthetically active radiation (FPAR), pi_mean, mh_mean and mh_gsrd_mean represent that the data are derived from their corresponding vegetation data. The "original" means using default original TM5-MP input data. The mixing ratios of CO_2 and CH_4 are fixed to 265.4 ppmv and 597.0 ppbv, respectively, for MH cases.

		pi_ctrl	pi_orig	pi_zero	mh	mh_gsrd
METEO	general	2009	2009	2009	2009	2009
	lsm	PD	PD	PD	MH	MH
	veg	pi_mean	2009	pi_mean	mh_mean	mh_gsrd_mean
EMISS	isoprene	pi_mean	2009	pi_mean	mh_mean	mh_gsrd_mean
	monoterpenes	pi_mean	2009	pi_mean	mh_mean	mh_gsrd_mean
	other natural	2009	2009	2009	2009	2009
	anthropogenic	1850	1850	zero	zero	zero
onlinedust	paleo-lakes	original	original	original	on	on
	FPAR	pi_mean	original	pi_mean	mh_mean	mh_gsrd_mean
	cultivation	zero	original	zero	zero	zero
CO_2		1850	1850	1850	264.4 ppmv	264.4 ppmv
CH_4		1850	1850	1850	597.0 ppbv	597.0 ppbv

data. The configuration of case pi_zero is the same as pi_ctrl except the anthropogenic emissions are switched off.

2.3 BVOC emission data from other sources

In order to compare our results with the simulated BVOC emissions from other models, we downloaded the model data from the *midHolocene* experiment in PMIP4-CMIP6, including *emivoc* (total emission rates of isoprene and monoterpenes) from NorESM2-LM and *emiisop* (emission rate of isoprene) from both NorESM2-LM and MRI-ESM2-0 (Zhang et al., 2019; Yukimoto et al., 2019). Currently, these are the only available BVOC emission data during MH published in PMIP4-CMIP6 database. The emission rate of monoterpenes from NorESM2-LM was calculated by subtracting *emiisop* from *emivoc*.

Furthermore, other available data from previous studies were also collected here (Table 2). Adams et al. (2001) estimated the global total annual emission rates of isoprene and monoterpenes in 5 ka, which were 666.5 and 137.6 $Tg\,a^{-1}$, respectively. Under the scenario of "present potential vegetation" (representing the PI vegetation), they estimated the isoprene emission rate as 561.4 $Tg\,a^{-1}$ and monoterpene emission rate as 116.5 $Tg\,a^{-1}$. Kaplan et al. (2006) simulated the emission rates of isoprene and monoterpenes as 516.4 $Tg\,C\,a^{-1}$ (585.3 $Tg\,a^{-1}$) and 117.6 $Tg\,C\,a^{-1}$ (133.3 $Tg\,a^{-1}$) for 6 ka, 540.7 $Tg\,C\,a^{-1}$ (612.8 $Tg\,a^{-1}$) and 121.3 $Tg\,C\,a^{-1}$ (137.5 $Tg\,a^{-1}$) for PI, respectively. Singarayer et al. (2011) calculated the time series of global isoprene emission rate over the last glacial cycle, and we estimated the value in 6 ka as about 860 $Tg\,C\,a^{-1}$ (974.7 $Tg\,a^{-1}$) and in present-day as about 950 $Tg\,C\,a^{-1}$ (1076.7 $Tg\,a^{-1}$) from their Fig. 1d.

As a comparison, Arneth et al. (2008) summarized previous studies and showed that the estimated ranges of present-day global total annual emissions of isoprene and monoterpenes are from 412 $Tg\,C\,a^{-1}$ (467 $Tg\,a^{-1}$) to 601 $Tg\,C\,a^{-1}$ (681 $Tg\,a^{-1}$) and from 32 $Tg\,C\,a^{-1}$ (36 $Tg\,a^{-1}$) to 127 $Tg\,C\,a^{-1}$ (144 $Tg\,a^{-1}$), respectively. More recent studies, including the estimation of present-day global total annual BVOC emissions, present a varied picture. Hantson et al. (2017), for example, showed an estimate of 385 $Tg\,C\,a^{-1}$ (436 $Tg\,a^{-1}$) and 28.6 $Tg\,C\,a^{-1}$ (32.4 $Tg\,a^{-1}$) for isoprene and monoterpenes. Meanwhile, Cao et al. (2021) presented a range of 411 to 473 $Tg\,C\,a^{-1}$ (466 to 536 $Tg\,a^{-1}$) for isoprene emissions across all CMIP6 models. Sindelarova et al. (2022) modeled various BVOC species in different CAMS-GLOB-BIO inventory versions, showing an isoprene emission range of 299.1 to 440.5 $Tg\,a^{-1}$ and a monoterpene emission range of 63.2 to 82.7 $Tg\,a^{-1}$. In the unit conversion between Tg C and Tg, the molar masses of 12, 68 and 136 $g\,mol^{-1}$ are assigned to carbon, isoprene and monoterpenes.

2.4 Marine sediment record

The reconstructed dust mass deposition flux data at different marine sediment sites in North Atlantic were collected for the comparison with model results. The sediment sites are shown in Fig. 1 and Table 3 with GC37, GC49, GC68 and ODP658C along the northwest African coast, VM20-234, GGC3 and GGC6 in the remote Atlantic Ocean and 103GGC in the

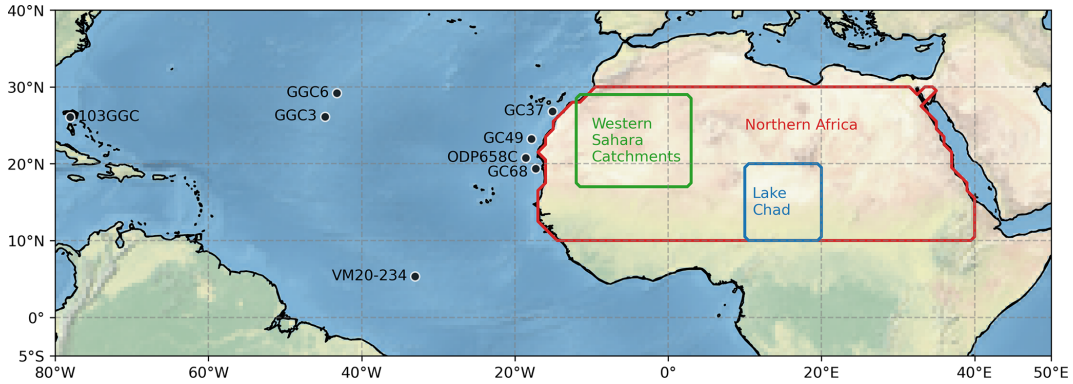

Figure 1. The marine sediment sites and the regions. The exact location of the sites are listed in Table 3. The red line encloses the northern Africa (NA) region, which is defined as the African continent area within the region 20° W to 40° E and 10 to 30° N. The blue box shows the Lake Chad (LC) region within 10–20° E and 10–20° N; the green box shows western Sahara catchments (WSC) region around the paleo-Lake Timbuktu area within 12° W–3° E and 17–29° N. The map was plotted with the Python matplotlib package, and the data points were generated by the authors.

Bahamas. The ^{230}Th (Thorium) normalization method was applied to calculate the dust fluxes at GC37, GC49, GC68 (McGee et al., 2013; Albani et al., 2015), ODP658C (Adkins et al., 2006), 103GGC and VM20-234 (Williams et al., 2016). The dust flux values at ODP658C were not given directly in the original references, so the terrigenous flux (F_{terr}) is calculated here with the original excess ^{230}Th (Ex^{230}Th) data according to the method in Adkins et al. (2006):

$$F_{\mathrm{terr}} = \frac{\beta z}{\mathrm{Ex}^{230}\mathrm{Th}} \cdot f_{\mathrm{terr}}, \tag{1}$$

where β is the production rate of ^{230}Th from ^{234}U in the water column, equal to 2.63×10^{-5} dpm cm^{-3} ka^{-1}, and dpm represents disintegration per minute, which is a radioactive decay unit. Here z is the water depth of the sediment core location, which is 2263 m (deMenocal et al., 2000) and f_{terr} is the fraction of the terrigenous flux out of the total sediment flux, which is set to 45 % for MH period and 60 % for PI period (see Table 2 in deMenocal et al., 2000). It should be noted that the terrigenous flux, which includes both the fluvial/shelf-derived and the eolian terrigenous flux, typically exceeds the dust flux. Therefore, we only compared the eolian terrigenous flux with the modeled dust flux (McGee et al., 2013). Similarly, the dust flux values at GGC3 and GGC6 were also not provided directly in Middleton et al. (2018), so these values (F_{dust}) were calculated from the original data as

$$F_{\mathrm{dust}} = \frac{[^4\mathrm{He}_{\mathrm{terr}}] \cdot \mathrm{vsr}}{5600}, \tag{2}$$

where [^{4}He$_{\mathrm{terr}}$] is the amount of terrigenous ^{4}He (Helium) in the sediment in units of ncc g^{-1} and ncc is equal to 10^{-9} cm^3 at standard temperature and pressure. vsr is vertical sediment rain rate in units of g cm^{-2} ka^{-1}; 5600 ncc g^{-1} is applied to convert the ^{4}He to ^{4}He-based dust fluxes.

Since the reconstructed sample ages are not exactly at PI (0.1 ka, 1850 compared to 1950) or MH (in our model simulations assumed to be 6 ka), the data closest to 0.1 nd 6 ka were selected. For the PI period, only the data younger than 1 ka were selected. For example, for GC49, the data in 0.55 ka was selected for PI and the data in 5.57 ka and 6.57 were selected for the MH period. Moreover, the estimated errors of 1 standard deviation of age and dust flux data were also collected whenever they were available in the literature.

2.5 Study domains

In this study, we defined three regions for detailed analysis besides the globe scale. Firstly, northern Africa (NA) is defined as the African continent area within the region 20° W to 40° E and 10 to 30° N. The other two regions are related to the paleo-waterbodies during MH where the dust emissions were reduced the most. One is the Lake Chad (LC) area within 10–20° E and 10–20° N and the other is the western Sahara catchments (WSC), centered around the paleo-Lake Timbuktu area within 12° W–3° E and 17–29° N. The two paleo-lakes are selected because the Lake Chad has been suggested to have thrived between 11 and 5 ka (Armitage et al., 2015), and Lake Timbuktu is considered to have experienced a wet period between 9.5 and 3.5 ka (Drake et al., 2022). The regions are shown on the map in Fig. 1 and the regional-average and summed values in Table 2 refer to the regions defined here.

3 Results and discussions

3.1 Surge in BVOC emissions

In the absence of available paleo-proxies to directly derive the BVOC emission data, we must rely on model simulations. Currently, the only available model results of BVOC emis-

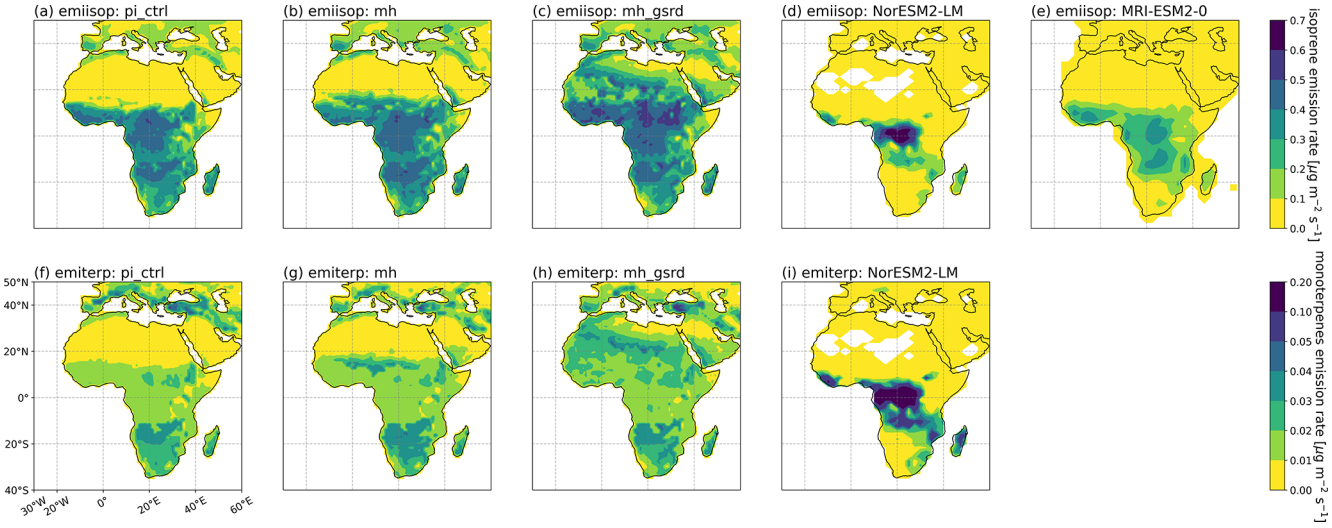

Figure 2. Annual mean emission rates of isoprene (emiisop) over Africa from the simulation cases pi_ctrl **(a)**, mh **(b)** and mh_gsrd **(c)**, as well as the PMIP4 simulation results of NorESM2-LM **(d)** and MRI-ESM2-0 **(e)**. The annual mean emission rates of monoterpenes (emiterp) are also shown for simulation cases pi_ctrl **(f)**, mh **(g)** and mh_gsrd **(h)** and the simulation results of NorESM2-LM **(i)**.

sions during MH from the PMIP4-CMIP6 midHolocene experiments come from NorESM2-LM and MRI-ESM2-0 simulations as mentioned above. Figure 2 shows the total annual emission rates of isoprene and monoterpenes from simulation cases pi_ctrl, mh and mh_gsrd in the present study, along with the results from NorESM2-LM and MRI-ESM2-0.

Due to the northward extension of vegetation cover over the NA region in the mh and mh_gsrd cases (elucidated in Lu et al., 2018), the emissions of both isoprene and monoterpenes increase compared to the pi_ctrl case (Fig. 2a–c and f–h). Notably, the BVOC emissions nearly cover the entire NA region in mh_gsrd (Fig. 2c and h). The total isoprene emissions over the NA region are 27.0, 50.5 and 114.8 $\mathrm{Tg\,a^{-1}}$ in pi_ctrl, mh and mh_gsrd, respectively. Correspondingly, the monoterpene emission rate is 2.3, 3.9 and 8.0 $\mathrm{Tg\,a^{-1}}$, respectively (Table 2). The relative increase in mh compared to pi_ctrl is 87 % for isoprene emissions and 70 % for monoterpene emissions, respectively. The mh_gsrd case, on the other hand, marks a more dramatic surge, with isoprene and monoterpene emissions increasing to 4.3 times and 3.5 times that of pi_ctrl, respectively.

Compared with the mh and mh_gsrd cases, the NorESM2-LM and MRI-ESM2-0 show lower isoprene emission rates over NA than the pi_ctrl case (Fig. 2a, d and e), which are 0.81 and 7.3 $\mathrm{Tg\,a^{-1}}$, respectively. Moreover, the BVOC emissions in these two models are mostly centered over central Africa, encompassing the present-day Congolian rainforest (Fig. 2d, e and i). In contrast, in our cases pi_ctrl, mh and mh_gsrd, in which the vegetation cover was simulated by the vegetation dynamic model LPJ-GUESS, the BVOC emissions are more evenly distributed over central and southern Africa, and they remain substantial at the southern end of Africa, reaching 0.4 $\mathrm{\mu g\,m^{-2}\,s^{-1}}$ for isoprene emissions and 0.03 $\mathrm{\mu g\,m^{-2}\,s^{-1}}$ for monoterpene emissions.

Besides the PMIP4-CMIP6 midHolocene experiment results, several studies have also provided estimates of BVOC emissions during the MH, as mentioned in Sect. 2.3. Among them, only Adams et al. (2001) reported a rise in isoprene emissions during MH compared to PI or present-day levels, in which the global total annual emission rate of isoprene increased by 19 % and of monoterpenes by 18 %, given the reconstructed vegetation cover. Moreover, in Fig. 1a and d in Adams et al. (2001) we can see that the area with isoprene emission rates larger than 2 $\mathrm{Tg\,M\,km^{-2}\,a^{-1}}$ (about 0.06 $\mathrm{\mu g\,m^{-2}\,s^{-1}}$, here the unit in Fig. 1 in Adams et al. (2001) is $\mathrm{Tg\,M\,ha^{-1}\,a^{-1}}$, but this is a typo and the correct unit is $\mathrm{Tg\,M\,km^{-2}\,a^{-1}}$) moves northward over NA in 5 ka, and the area with emissions greater than 15 $\mathrm{Tg\,M\,km^{-2}\,a^{-1}}$ (about 0.48 $\mathrm{\mu g\,m^{-2}\,s^{-1}}$) increased in the Sahel region.

In this study, the total annual global emissions of isoprene and monoterpenes are 889.7 and 74.3 $\mathrm{Tg\,a^{-1}}$ in the mh_gsrd case and 688.0 and 61.4 $\mathrm{Tg\,a^{-1}}$ in the pi_ctrl case, respectively. These values align with the higher BVOC emissions during the MH similar with that in Adams et al. (2001). Conversely, Kaplan et al. (2006) noted lower BVOC emissions in 6 ka, with 585.3 $\mathrm{Tg\,a^{-1}}$ for isoprene and 133.3 $\mathrm{Tg\,a^{-1}}$ for monoterpenes compared to 612.8 and 137.5 $\mathrm{Tg\,a^{-1}}$ during the PI period. They also specified that their vegetation simulations could not reproduce the northward shift of vegetation over Sahara region, likely due to their climate model (HCUM, Hadley Centre Unified Model) unable to capture the interactive processes between land, atmosphere and ocean. Singarayer et al. (2011) also showed a decreasing trend of global isoprene emission rate from the PI period to the MH period. Moreover, to our knowledge, no recent studies have

Table 2. Global- and regional-averaged values and summed values of different quantities for the simulation cases pi_ctrl, pi_zero (only for sconcccn020), mh and mh_gsrd, as well as other data sources, including noresm (NorESM2-LM PMIP4 midHolocene experiment), mriesm (MRI-ESM2-0 PMIP4 midHolocene experiment), A2001 (Adams et al., 2001), K2006 (Kaplan et al., 2006) and S2011 (Singarayer et al., 2011). The values listed are annual area-summed values of emiisop (isoprene emission rate, $\mathrm{Tg\,a^{-1}}$), emiterp (emission rate of monoterpenes, $\mathrm{Tg\,a^{-1}}$), emidust (dust emission rate, $\mathrm{Tg\,a^{-1}}$) and depdust (dust deposition rate, $\mathrm{Tg\,a^{-1}}$); annual area-summed values of loaddust (dust load, Tg) and loadsoa (SOA load, Tg); annual area-averaged mean values of sconcdust (surface mass concentration of dust, $\mu\mathrm{g\,m^{-3}}$), sconcsoa (surface mass concentration of SOA, $\mu\mathrm{g\,m^{-3}}$), sconcccn020 (surface concentration of CCN at supersaturation of 0.20 %, $\mathrm{cm^{-3}}$), od550aer (aerosol optical depth (AOD) at 550 nm), od550soa (SOA AOD at 550 nm) and od550dust (dust AOD at 550 nm).

Variable name	Case	Region			
		Global	Northern Africa	Lake Chad	Western Sahara catchments
emiisop	pi_ctrl	688.0	27.0	3.4	1.6
	mh	757.6	50.5	9.2	3.7
	mh_gsrd	889.7	114.8	13.5	16.5
	noresm	446.4	0.81	0.090	0.0043
	mriesm	466.3	7.3	1.5	0.073
	A2001, PI	561.4	NA	NA	NA
	A2001, 5 ka	666.5	NA	NA	NA
	K2006, PI	612.8	NA	NA	NA
	K2006, 6 ka	585.3	NA	NA	NA
	S2011, PD	1076.7	NA	NA	NA
	S2011, 6 ka	974.7	NA	NA	NA
emiterp	pi_ctrl	61.4	2.3	0.31	0.16
	mh	67.5	3.9	0.70	0.37
	mh_gsrd	74.3	8.0	0.79	1.5
	noresm	96.8	0.12	0.0060	0.00026
	mriesm	NA	NA	NA	NA
	A2001, PI	116.5	NA	NA	NA
	A2001, 5 ka	137.6	NA	NA	NA
	K2006, PI	137.5	NA	NA	NA
	K2006, 6 ka	133.3	NA	NA	NA
depdust	pi_ctrl	855.4	135.0	36.4	28.4
	mh	664.8	54.0	5.1	12.7
	mh_gsrd	594.8	21.3	2.5	4.0
emidust	pi_ctrl	854.9	280.6	80.1	82.1
	mh	665.9	95.0	2.8	25.2
	mh_gsrd	596.1	26.8	2.9	5.2
sconcdust	pi_ctrl	4.7	89.0	203.2	99.6
	mh	3.2	33.1	31.8	38.0
	mh_gsrd	2.8	15.9	15.6	15.1
loaddust	pi_ctrl	9.2	2.1	0.41	0.45
	mh	6.1	0.77	0.10	0.17
	mh_gsrd	5.2	0.37	0.044	0.068
sconcsoa	pi_ctrl	3.2	1.0	1.3	0.80
	mh	3.6	1.5	2.2	1.2
	mh_gsrd	4.3	2.9	3.9	2.8
loadsoa	pi_ctrl	1.3	0.066	0.0096	0.011
	mh	1.4	0.091	0.014	0.015
	mh_gsrd	1.6	0.15	0.023	0.029
sconcccn020	pi_zero	0.00051	96.2	110.2	74.1
	pi_ctrl	0.00063	127.7	138.7	99.4
	mh	0.00053	103.2	120.6	79.6
	mh_gsrd	0.00054	112.6	130.3	92.0
od550aer	pi_ctrl	6.8×10^{-7}	0.212	0.323	0.211
	mh	6.2×10^{-7}	0.122	0.146	0.116
	mh_gsrd	6.4×10^{-7}	0.132	0.156	0.124
od550dust	pi_ctrl	1.6×10^{-7}	0.147	0.247	0.155
	mh	1.1×10^{-7}	0.048	0.054	0.051
	mh_gsrd	9.6×10^{-8}	0.026	0.027	0.024
od550soa	pi_ctrl	1.2×10^{-7}	0.032	0.040	0.027
	mh	1.3×10^{-7}	0.045	0.059	0.038
	mh_gsrd	1.6×10^{-7}	0.077	0.096	0.074

NA stands for not available.

probed the BVOC emissions during the MH, despite Adams et al. (2001) proposing about 2 decades ago that such exploration could significantly enhance our understanding of past climate change.

3.2 Reduced dust emission

In order to verify our model simulation results, especially concerning new dust emission configurations, the modeled dust deposition fluxes were compared with the reconstructed data (Fig. 3). For the PI period, the model results agree well with the proxy data at GC49 and 103GGC (Fig. 3a). At ODP658C, the model result is only 59 % of the proxy data (Table 3). However, it should be noted that the dust flux at ODP658C may also include a fluvial/shelf-derived flux, estimated to be about 34 % of the actual dust flux as seen at the nearby site GC68 (see Fig. 3 in McGee et al., 2013). Consequently, the estimated actual dust flux at ODP658C during the PI is about $11.87\,\mathrm{g\,m^{-2}\,a^{-1}}$, closely aligning with our model result $10.63\,\mathrm{g\,m^{-2}\,a^{-1}}$. The model result at VM20-234 (Fig. 3a) should not be viewed as an overestimation but rather as consistent with the increasing trend of dust flux as we approach the PI era from 0.97 ka (see Fig. 2d in Williams et al., 2016).

During the MH period, the model results of both mh and mh_gsrd consistently reproduce the low dust fluxes at the remote sites, such as VM20-234, 103GGC, GGC3 and GGC6, despite underestimating the proxy data at VM20-234 (Fig. 3b). For the sites GC37, GC49 and GC68 along the northwest Africa coast, the model results in the mh case are consistent with the proxy data at GC37 but highly overestimate the values at GC49 and GC68 by about 3 to 4 times (Table 3). The mh_gsrd case, on the other hand, matches the proxy data at GC49 and GC68 but underestimates the value

Table 3. Reconstructed and modeled dust mass deposition fluxes (DMDF) at different sites. The references of reconstructed data are listed below the table. The estimated errors in reconstructed data are shown in the brackets if they are provided in the original references.

Site	Lat (° N)	Long (° W)	Reconstructed data age (ka)	Reconstructed DMDF ($g\,m^{-2}\,a^{-1}$)	Modeled DMDF ($g\,m^{-2}\,a^{-1}$) pi_ctrl	mh	mh_gsrd
GC37[1]	26.82	15.12	6.22 (±0.23)	0.92 (±0.14)	1.56	0.94	0.32
GC49[1]	23.21	17.85	0.55 (±0.24) 5.57 (±0.34) 6.57 (±0.08)	5.70 (±0.89) 1.11 (±0.17) 1.23 (±0.19)	5.51	4.21	0.78
GC68[1]	19.36	17.28	5.89 (±0.14) 6.30 (±0.24)	4.00 (±0.68) 3.67 (±0.65)	16.56	11.36	3.70
ODP658C[2]	20.75	18.58	0.193 5.808 6.057	17.990 8.554 8.901	10.63	7.66	2.20
VM20-234[3]	5.33	33.03	0.97 6.03	2.96 (±0.13) 1.66 (±0.07)	4.40	1.22	0.66
103GGC[3]	26.07	78.06	0.29 5.88	0.82 (±0.06) 0.53 (±0.04)	0.86	0.43	0.22
GGC3[4]	26.14	44.80	6.0	0.22	0.86	0.34	0.13
GGC6[4]	29.21	43.23	0.5 6.2	0.29 0.14	0.57	0.26	0.15

[1] McGee et al. (2013), Albani et al. (2015). [2] deMenocal et al. (2000), Adkins et al. (2006). [3] Williams et al. (2016). [4] Middleton et al. (2018).

at GC37 (Fig. 3b). This indicates that the reduction in dust emissions due to the existence of waterbodies over the WSC region may be overestimated in the mh_gsrd simulation. As for ODP658C, as mentioned above, the reconstructed dust flux may exceed the actual value, and here the actual flux is estimated as 1/2 to 1/3 of the original value based on the observation at sites GC66 (19.944° N, 17.860° W) and GC68 (see Fig. 3 in McGee et al., 2013), yielding an estimate of about 2.91 to 4.36 $g\,m^{-2}\,a^{-1}$. Therefore, based on the estimation, while the mh case drastically overestimates the proxy data, the mh_gsrd case underestimates the value but agrees better than mh (Table 3). The comparison results affirm that the new dust emission configuration in the model is able to predict the dust flux pattern during both PI and MH periods, as demonstrated by the pi_ctrl and mh_gsrd cases, respectively, across a substantial expanse stretching from the west Atlantic Ocean to the northwest coast of Africa.

Figure 4a shows that during the PI, the simulated dust emissions occur over the entire NA region, especially the Sahara region, reaching over 100 $g\,m^{-2}\,a^{-1}$ in the regions such as LC, WSC and northern Algeria. However, during the MH the dust emissions decreased significantly, especially in the paleo-lake regions LC and WSC, where the total annual dust emissions are 2.9 and 5.2 $Tg\,a^{-1}$ in mh_gsrd and 2.8 and 25.2 $Tg\,a^{-1}$ in mh, respectively (Table 2).

The values of mh align closely in magnitude with the model results from Egerer et al. (2018) for 6 ka, but the annual dust emissions in the WSC region from the mh_gsrd case are only about 1 / 10 that over the similar western Sahara region in Egerer et al. (2018). This discrepancy could result from, besides the paleo-lake configuration, that we also set the FPAR values with reconstructed vegetation cover, which reduced the local dust emissions further. Later, when the paleo-lakes eventually dried out, the exposed slit material became vulnerable to surface wind, transforming the surrounding area into a major dust source (Tegen et al., 2002). This led to increased dust emissions during the PI period, resulting in 80.1 $Tg\,a^{-1}$ over the LC region and 82.1 $Tg\,a^{-1}$ over the WSC region under the pi_ctrl case (Table 2). Consequently, dust emissions are reduced by about 96 % and 94 % in the LC and WSC regions, respectively. Considering that the dust emissions in the default PI case pi_orig are even higher than in pi_ctrl (Fig. 4b), the relative reduction in dust emissions during the MH period compared to the PI period could be more pronounced.

The reduced dust emissions thus lead to a wide range of reduced surface dust concentration and dust load due to air-mass transport over NA during the MH period (Fig. 5). The most notable reduction in dust load in both the mh and mh_gsrd cases occurs over the LC and WSC regions, reflect-

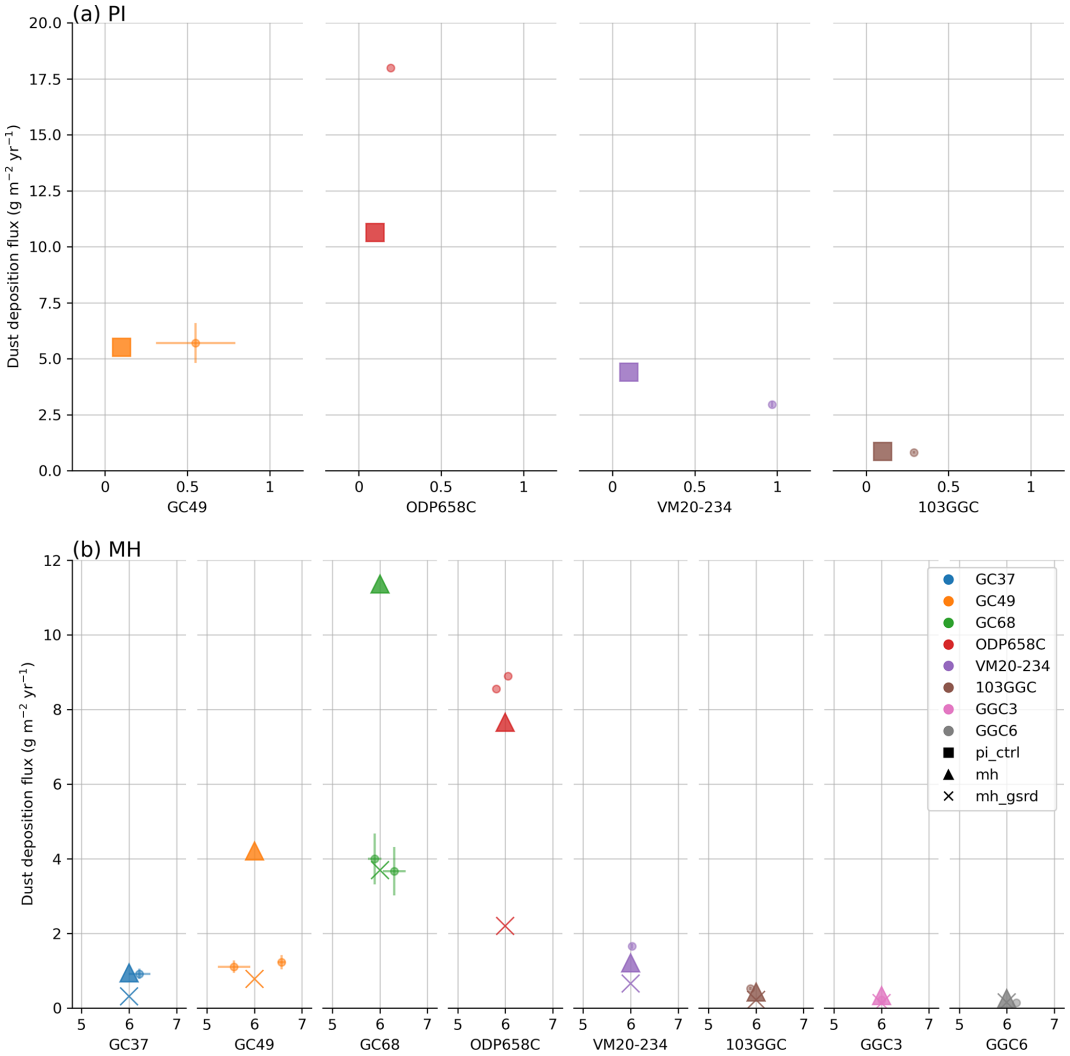

Figure 3. Reconstructed (circles) and modeled (square for pi_ctrl, triangle for mh and cross for mh_gsrd) dust deposition fluxes during **(a)** PI and **(b)** MH periods. Different colors are set for different sediment sites which are shown in the legend. The x axis shows the age in units of ka. The error bars of dust fluxes are plotted for GC37, GC49, GC68, VM20-234 and 103GGC, and the age error bars are plotted for GC37, GC49 and GC68.

ing the dust emission differential pattern (Fig. 5d and f). The surface dust concentration closely correlated with dust load. When compared to pi_ctrl, the annual mean of these two variables over NA declined by 63 % in mh and 82 % in mh_gsrd, respectively. And interestingly, the relative reduction in dust load in the mh_gsrd case corresponds with the prescribed reduction percentage of dust mixing ratio below 150 hPa over NA in Pausata et al. (2016). This report provided the original MH climate forcing conditions for the dynamic vegetation simulations in Lu et al. (2018).

3.3 Increased SOA

In TM5-MP, isoprene and monoterpenes are the sole precursors of SOA formation (Bergman et al., 2022). Therefore, the modeled surface concentration of SOA mirrors the emission rates of isoprene and monoterpenes in individual cases (Fig. 6a, c and e).

In the pi_ctrl case, the peak SOA surface concentration appears in central Africa along the longitude 20° E from around 0 to 10° N, with the highest values exceeding 2.5 µg m^{-3} (Fig. 6a). In the mh case, SOA surface concentration increases due to higher BVOC emissions over the Sahel region with the highest recorded values exceeding 3.0 µg m^{-3} (Fig. 6c). Moreover, the northernmost region of maximum concentration extends further in this case compared to pi_ctrl, but it is primarily confined to a narrow belt between 10 and 20° N, reflecting the less northward extension of BVOC emissions. Here the average relative increase in SOA surface concentration over the NA region is 50 % compared to pi_ctrl (Fig. 6d).

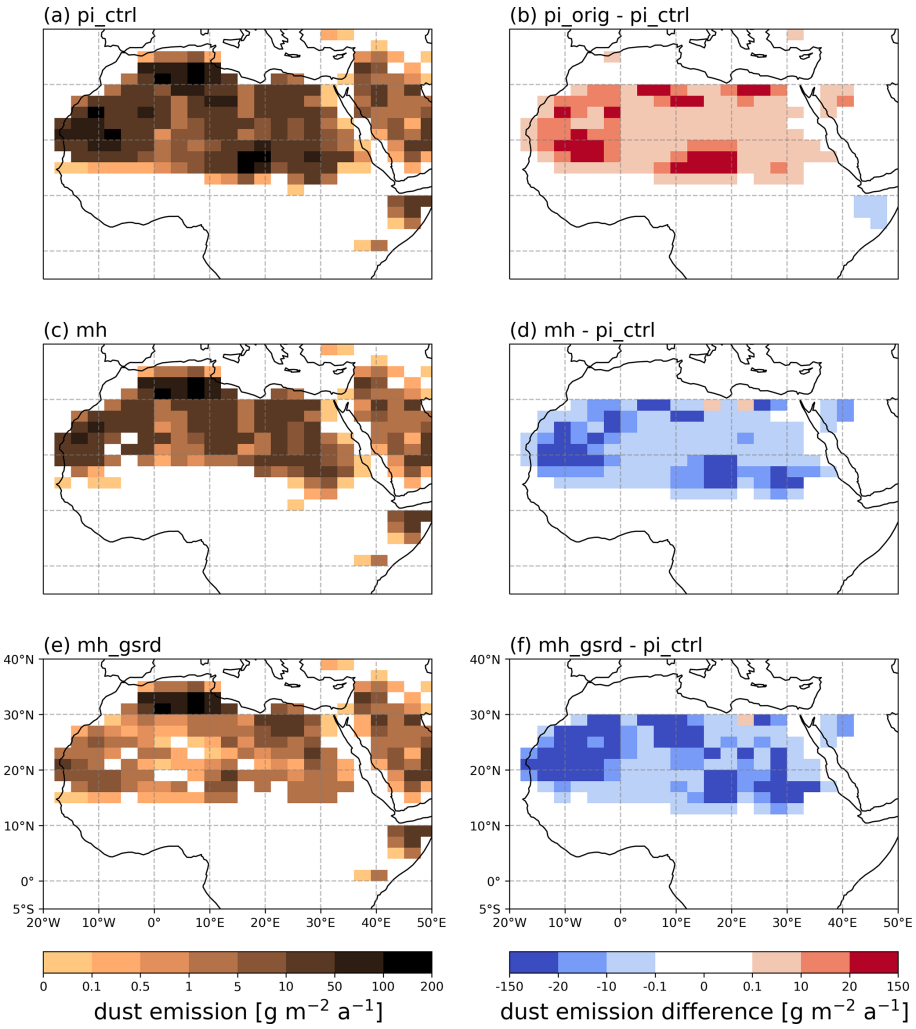

Figure 4. Global annual dust emissions in units of g m^{-2} a^{-1} over central and northern Africa in the pi_ctrl **(a)**, mh **(c)** and mh_gsrd **(e)** cases, as well as the dust emission differences between pi_orig and pi_ctrl **(b)**, mh and pi_ctrl **(d)** and mh_gsrd and pi_ctrl **(f)**, respectively.

While in the mh_gsrd case, as the vegetation covers nearly the whole of Africa, especially the NA region compared to the other two cases, the SOA surface concentration is higher than 4.5 µg m^{-3} across western to central Africa (Fig. 6e). The significantly increased BVOC emissions due to northward extension of vegetation cover result in a more than 1 µg m^{-3} greater SOA surface concentration over nearly the entire NA region in mh_gsrd compared to pi_ctrl. The difference increases to over 2 µg m^{-3} across the western and central areas, resulting in a value 2.9 times greater than that in the pi_ctrl case over the NA region (Fig. 6f). Figure 6b shows that SOA surface concentration is lower in central Africa in pi_ctrl compared to original PI simulation case pi_orig. This indicates that over this area, the simulated SOA concentration during the MH period is lower than that in the pi_orig case due to lower vegetation cover.

3.4 Impact on size distributions and CCN

In order to estimate the potential impact of the increased SOA formation over NA region on cloud properties, we examined the CCN surface concentrations at supersaturations of 0.2 % (CCN0.2) (Fig. 7), which are roughly related to the number concentrations of particles larger than 100 to 200 nm (Jokinen et al., 2015). Within this size range, the CCN0.2 concentration is mainly determined by particles in the soluble accumulation (ACS) mode and soluble coarse (COS) mode (Figs. S3 and S4). Nevertheless, during the PI period, anthropogenic primary aerosol emissions from Europe enhanced the particle number concentration in ACS mode and consequently the CCN0.2 concentration (Fig. 7a and b), exceeding the impact of land cover change during the MH. Therefore, we conducted another simulation pi_zero which is the same as pi_ctrl but without any anthropogenic emissions. Compared to pi_zero, the average CCN0.2 surface concen-

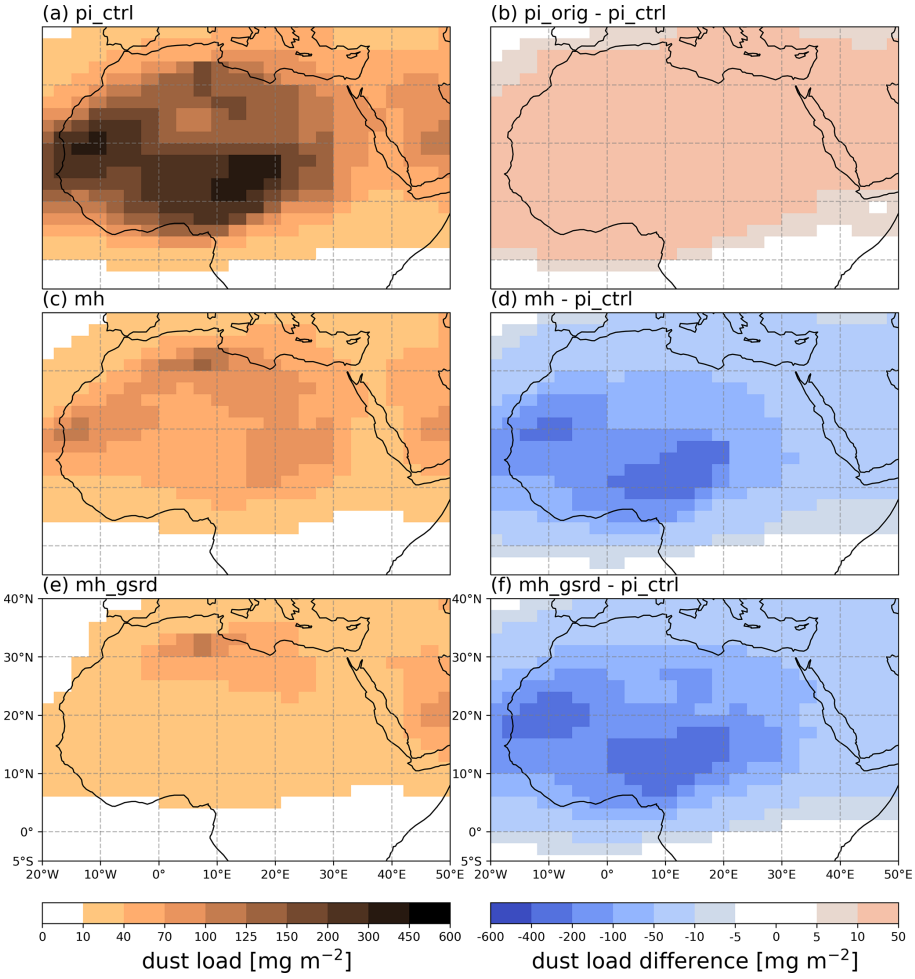

Figure 5. Same as Fig. 4 but for dust load in units of mg m^{-2}.

tration over NA in mh and mh_gsrd increased by about 7 % and 17 %, respectively.

The reduced dust emissions during the MH period decreased the mass concentration of COS mode over the NA region, but the number concentration was unaffected (Figs. S3 and S4). Concurrently, over the same region, the number concentration of ACS mode increased (Fig. 7e and h) due to the enhanced SOA concentration, which exceeded the impact of decreased sulfate concentration (Figs. S3 and S4), leading to increased CCN0.2 concentration (Fig. 7d and g). However, the hygroscopicity parameter of SOA is only 0.1 while for sulfate it is 0.6, so the CCN0.2 number concentration only increased by less than 10 and 20 cm^{-3} over the NA region in mh and mh_gsrd, respectively. It should be noted that the enhanced BVOC emissions not only increased SOA concentration but also consumed more OH (hydroxyl radical) via the oxidation reactions. Figure 7f and i show that the OH number concentration over the NA region in mh and mh_gsrd decreases more than 20 % and 60 % compared to the pi_zero case, respectively. This leads to reduced gas-phase sulfuric acid concentration which is produced mainly via the reaction between SO_2 (sulfur dioxide) and OH, and finally leads to lower sulfate concentration.

Figure 7e and h show a decrease in the ACS mode in central Africa in the mh and mh_gsrd cases, yet the CCN0.2 number concentration still shows positive change. The reduction in the number concentration of the ACS mode is mainly attributed to the decreased BC (black carbon) and POM (primary organic matter) (Figs. S3 and S4), which have hygroscopicity parameters of 0 and 0.1, respectively. Therefore, although the number concentration of ACS mode decreases, the average hygroscopicity of the particles could still increase due to the significant enhancement of SOA concentration over this region. Moreover, the average diameter of the ACS mode may not be affected due to the counteraction between the increased SOA concentration and the decreased concentrations of BC and POM.

In general, the enhanced BVOC emissions due to vegetation cover change are able to affect the cloud properties (e.g., reflectivity, lifetime and precipitation properties) via increas-

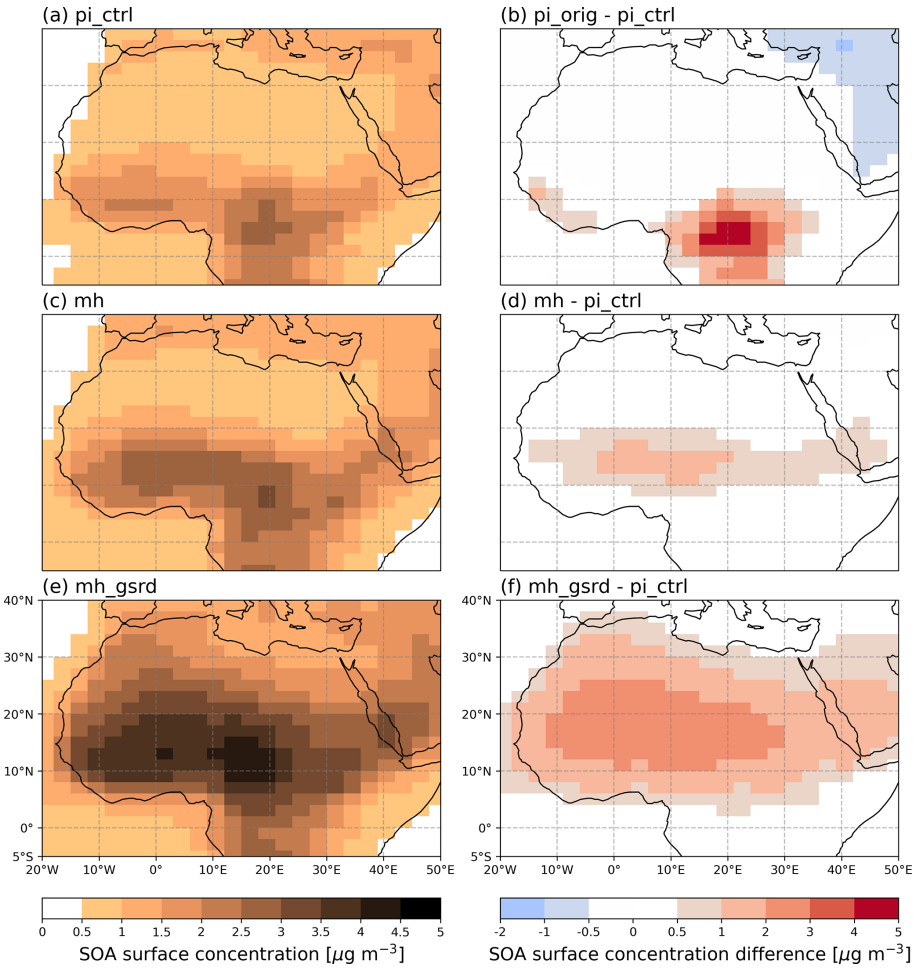

Figure 6. Same as Fig. 4 but for SOA surface concentration in units of $\mu g\,m^{-3}$.

ing CCN concentrations over the NA region, which needs to be kept in mind in future studies. Moreover, because of the complex consequences originating from the changed BVOC emissions as mentioned above, one should be careful when analyzing the aerosol–cloud interactions.

3.5 Reduction in AOD

During the PI period, the aerosol optical depth at 550 nm (AOD550) over NA is dominantly affected by the dust load (Figs. 8a and 5a). The dust emission source areas surrounding LC region show the highest aerosol optical depth, exceeding 0.3. During the MH, these areas along with their downwind locations show the largest reduction in AOD550 at around −0.3 in both mh and mh_gsrd cases (Fig. 8d and f). Both cases demonstrate similar patterns of AOD550 variation over NA. Interestingly, although the dust load in mh_gsrd is about 51.9 % lower than that in mh over NA region, the AOD550 in mh_gsrd remains 0.01 higher, which is about 8.2 % increase compared to that in mh. This suggests that the AOD550 increase due to the increasing of SOA surpasses the AOD550 reduction due to the decrease in dust. For example, in the mh case, the AOD550 over the NA region is split between 0.048 (51.6 %) for dust and 0.045 (48.4 %) for SOA, while in the mh_gsrd case, the values shift to 0.026 (25.2 %) and 0.077 (74.8 %), respectively. Given that mh_gsrd is the more realistic case, neglecting the AOD550 change due to the increased SOA over NA during the MH would result in underestimating the AOD550 by 0.045 (i.e., 0.077 minus 0.032). This accounts for about 21.2 % of AOD550 in pi_ctrl case. Our result of AOD550 for dust over the NA region in mh_gsrd is 0.026, which aligns with the simulation result of "MH control" (0.02 over Sahara) as presented in Thompson et al. (2019).

4 Conclusion

In this study, we produced a new dataset of emissions of isoprene and monoterpenes, and we also refined the methodology for calculating the dust emissions over northern Africa during the mid-Holocene period. The updated emission data were derived from the simulated vegetation cover data from

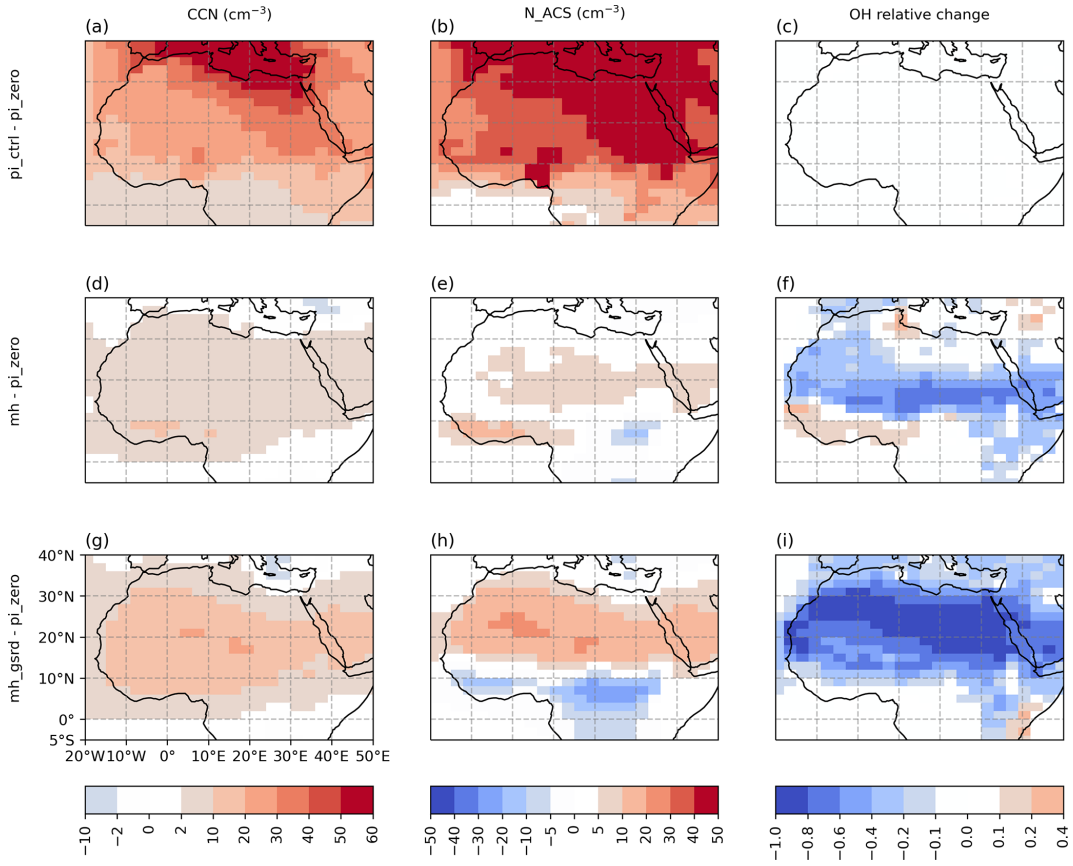

Figure 7. The difference in **(a)** CCN at supersaturation of 0.2 % in units of cm^{-3}, **(b)** number concentration of particles in the soluble accumulation mode (N_ACS) in units of cm^{-3} between pi_ctrl and pi_zero. **(c)** The relative change in OH surface number concentration in pi_ctrl compared to pi_zero. The same for **(d, g)** CCN, **(e, h)** N_ACS and **(f, i)** OH relative change but between mh and pi_zero, mh_gsrd and pi_zero, respectively.

Lu et al. (2018), which were found to be closely aligned with the reconstructed proxy data in Hély et al. (2014). Due to the northward expansion of grassland and trees, the total annual emission rate over the NA region increased from 27.0 Tg a^{-1} during the PI period (pi_ctrl) to 114.8 Tg a^{-1} during the MH period (mh_gsrd) for isoprene and from 2.3 to 8.0 Tg a^{-1} for monoterpenes. When compared with results from previous studies and PMIP4 simulations, our new dataset more accurately reflects the land cover change during the MH, which has been shown in Lu et al. (2018). Moreover, our finding of increased BVOC emissions during the MH period aligns with the results from Adams et al. (2001), who also calculated BVOC emissions from reconstructed vegetation cover.

Furthermore, the increased vegetation cover over northern Africa resulted in decreased annual dust emissions within this area from 280.6 Tg a^{-1} during the PI period (pi_ctrl) to 26.8 Tg a^{-1} during the MH period (mh_gsrd). Of the reduction, the LC and WSC regions contributed to 77.2 and 76.9 Tg a^{-1}, respectively, altogether accounting for roughly 60.7 % of the total reduction. It is noteworthy that these two regions (LC and WSC) were marked by the presence of actual waterbodies instead of preferential dust emission spots covered by silt and clay soil materials (Tegen et al., 2002; Egerer et al., 2018). Our model configuration of dust emissions was also evaluated by the agreement between the modeled and reconstructed dust deposition fluxes at different marine sediment locations across the Atlantic Ocean.

The decreased dust emissions in mh_gsrd resulted in a significant 82.4 % reduction in dust load and a comparable 82.3 % reduction in dust AOD550. However, enhanced SOA formation from increased BVOC emissions also increased the AOD550, which ultimately caused the lesser total AOD550 reduction of 37.7 %. Furthermore, the increased SOA surface concentration and load increased the CCN0.2 number concentration near the surface over the NA region by 7 % and 17 % in mh and mh_gsrd cases, respectively, compared to the PI period. This could potentially influence the regional climate via aerosol–cloud interactions. Nevertheless, our findings suggest that this may not be an efficient feedback pathway due to the counteracting effects originating from enhanced BVOC emissions.

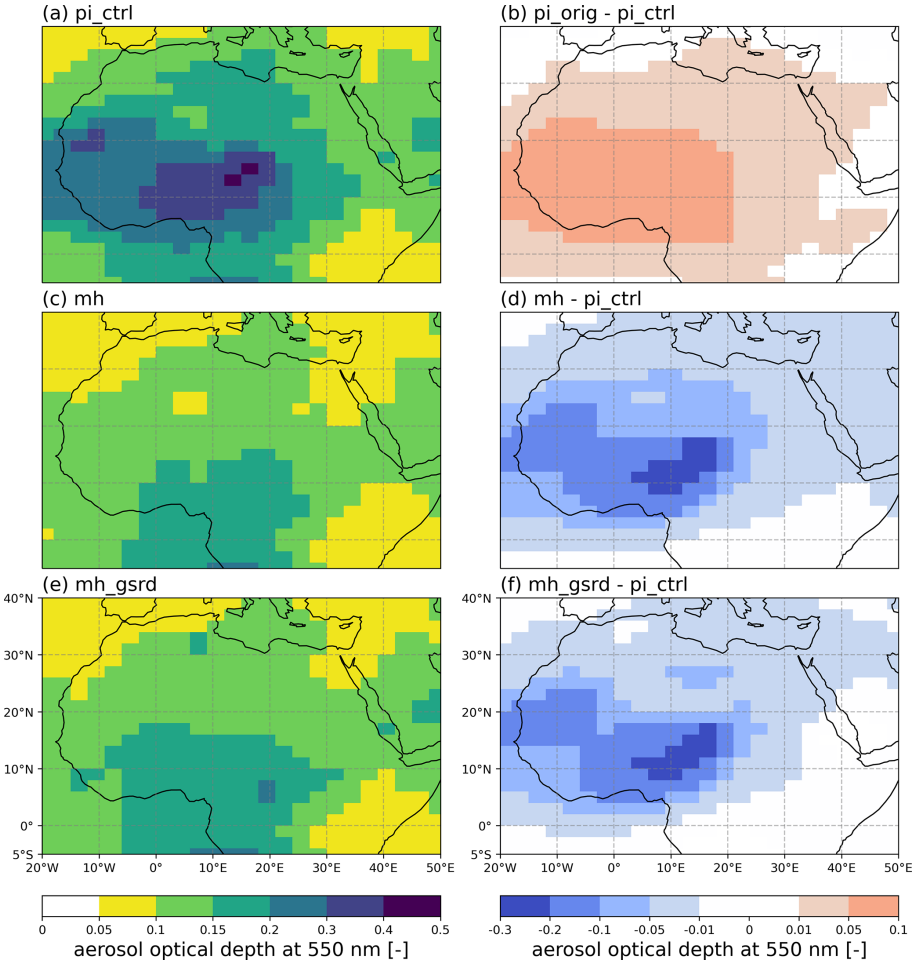

Figure 8. Same as Fig. 4 but for aerosol optical depth at 550 nm.

Additionally, we have not analyzed the impact of the changing meteorology during the MH compared to present-day over NA, which is beyond the scope of this study. Nevertheless, it should be kept in mind that a reduced eastward wind pattern over NA as demonstrated by previous studies (e.g., Pausata et al., 2016; Williams et al., 2020) and increased rainfall could alter the transportation and wet deposition processes. Hence, more comprehensive investigations using coupled Earth system model simulations are needed to quantify how these processes altogether impact precipitation and regional climate.

Considering BVOC's critical role in atmosphere–biosphere interactions as precursors of SOA (Kulmala et al., 2014; Yli-Juuti et al., 2021), more consistent BVOC emissions and consequently SOA formation will improve the simulation of the MH period, especially over northern Africa in future model experiments. The findings of this study serve as a valuable reference point for the emissions of isoprene, monoterpenes and dust in future MH model simulations, as will be defined in, e.g., PMIP5.

Code and data availability. The TM5-MP source code, modified model input data and the model output data are available at Zenodo (https://doi.org/10.5281/zenodo.8410150) (Zhou et al., 2023). Access to the latest version of TM5-MP in the GitLab repository can be obtained from Philippe Le Sager (philippe.le.sager@knmi.nl).

Supplement. The supplement related to this article is available online at: https://doi.org/10.5194/cp-19-2445-2023-supplement.

Author contributions. RM and PTZ proposed the paper idea. PTZ processed the datasets, conducted the model configurations and simulations, analyzed the results, plotted the figures and wrote the article. ZYL provided the LPJ-GUESS data and contributed to processing the data. JPK contributed to model configurations and simulations on CSC supercomputers. JL, TVN and PLS contributed to model configurations. All authors provided comments and contributed to paper discussion and writing.

Competing interests. The contact author has declared that none of the authors has any competing interests.

Disclaimer. Publisher' note: Copernicus Publications remains neutral with regard to jurisdictional claims made in the text, published maps, institutional affiliations, or any other geographical representation in this paper. While Copernicus Publications makes every effort to include appropriate place names, the final responsibility lies with the authors.

Acknowledgements. We thank CSC (IT Center for Science, Finland) for computational resources.

Financial support. We acknowledge University of Helsinki Three Year Grant AGES, eSTICC (272041), the Academy of Finland Centre of Excellence (307331), the funding from EU H2020 project FORCeS (grant agreement no. 821205), the ACCC Flagship funded by the Academy of Finland (grant number 337549 for UH, and grant number 337552 for FMI), the Autumn 2020 Arctic Avenue (spearhead research project between the University of Helsinki and Stockholm University), the European Commission Horizon Europe project FOCI (Non-CO_2 Forcers and Their Climate, Weather, Air Quality and Health Impacts, grant agreement no. 101056783) and the project GRASS (Green Sahara: a cross-disciplinary approach to modelling climate and human distribution) funded by the Academy of Finland. Qiong Zhang acknowledges the support from the Swedish Research Council (Vetenskapsrådet, grant no. 2017-04232). Additional funding was provided to Zhengyao Lu by the Swedish Research Council Formas (grant no. 2020-02267), and the Swedish Research Council Vetenskapsrådet (grant no. 2022-03617). The LPJ-GUESS data processing was enabled by resources provided by the National Academic Infrastructure for Supercomputing in Sweden (NAISS) and the Swedish National Infrastructure for Computing (SNIC) partially funded by the Swedish Research Council through grant agreements nos. 2022-06725 and 2018-05973.

Open-access funding was provided by the Helsinki University Library.

Review statement. This paper was edited by Z. S. Zhang and reviewed by Yonggang Liu and Yong Sun.

References

Adams, J. M., Constable, J. V., Guenther, A. B., and Zimmerman, P.: An estimate of natural volatile organic compound emissions from vegetation since the last glacial maximum, Chemosphere, 3, 73–91, 2001.

Adkins, J., deMenocal, P., and Eshel, G.: The "African humid period" and the record of marine upwelling from excess ^{230}Th in Ocean Drilling Program Hole 658C, Paleoceanography, 21, PA4203, https://doi.org/10.1029/2005PA001200, 2006.

Albani, S., Mahowald, N. M., Winckler, G., Anderson, R. F., Bradtmiller, L. I., Delmonte, B., François, R., Goman, M., Heavens, N. G., Hesse, P. P., Hovan, S. A., Kang, S. G., Kohfeld, K. E., Lu, H., Maggi, V., Mason, J. A., Mayewski, P. A., McGee, D., Miao, X., Otto-Bliesner, B. L., Perry, A. T., Pourmand, A., Roberts, H. M., Rosenbloom, N., Stevens, T., and Sun, J.: Twelve thousand years of dust: the Holocene global dust cycle constrained by natural archives, Clim. Past, 11, 869–903, https://doi.org/10.5194/cp-11-869-2015, 2015.

Armitage, S. J., Bristow, C. S., and Drake, N. A.: West african monsoon dynamics inferred from abrupt fluctuations of lake megachad, P. Natl. Acad. Sci. USA, 112, 8543–8548, 2015.

Arneth, A., Monson, R. K., Schurgers, G., Niinemets, Ü., and Palmer, P. I.: Why are estimates of global terrestrial isoprene emissions so similar (and why is this not so for monoterpenes)?, Atmos. Chem. Phys., 8, 4605–4620, https://doi.org/10.5194/acp-8-4605-2008, 2008.

Bergman, T., Makkonen, R., Schrödner, R., Swietlicki, E., Phillips, V. T. J., Le Sager, P., and van Noije, T.: Description and evaluation of a secondary organic aerosol and new particle formation scheme within TM5-MP v1.2, Geosci. Model Dev., 15, 683–713, https://doi.org/10.5194/gmd-15-683-2022, 2022.

Cao, Y., Yue, X., Liao, H., Yang, Y., Zhu, J., Chen, L., Tian, C., Lei, Y., Zhou, H., and Ma, Y.: Ensemble projection of global isoprene emissions by the end of 21st century using CMIP6 models, Atmos. Environ., 267, 118766, https://doi.org/10.1093/acrefore/9780190228620.013.532, 2021.

Carslaw, K. S., Boucher, O., Spracklen, D. V., Mann, G. W., Rae, J. G. L., Woodward, S., and Kulmala, M.: A review of natural aerosol interactions and feedbacks within the Earth system, Atmos. Chem. Phys., 10, 1701–1737, https://doi.org/10.5194/acp-10-1701-2010, 2010.

Chandan, D. and Peltier, W. R.: African Humid Period Precipitation Sustained by Robust Vegetation, Soil, and Lake Feedbacks, Geophys. Res. Lett., 47, e2020GL088728, https://doi.org/10.1029/2020GL088728, 2020.

Claussen, M., Dallmeyer, A., and Bader, J.: Theory and modeling of the African humid period and the green Sahara, in: Oxford Research Encyclopedia of Climate Science, Oxford University Press, https://doi.org/10.1093/acrefore/9780190228620.013.532, 2017.

Dee, D. P., Uppala, S. M., Simmons, A. J., Berrisford, P., Poli, P., Kobayashi, S., Andrae, U., Balmaseda, M. A., Balsamo, G., Bauer, P., Bechtold, P., Beljaars, A. C. M., van de Berg, L., Bidlot, J., Bormann, N., Delsol, C., Dragani, R., Fuentes, M., Geer, A. J., Haimberger, L., Healy, S. B., Hersbach, H., Hólm, E. V., Isaksen, L., Kållberg, P., Köhler, M., Matricardi, M., McNally, A. P., Monge-Sanz, B. M., Morcrette, J.-J., Park, B.-K., Peubey, C., de Rosnay, P., Tavolato, C., Thépaut, J.-N., and Vitart, F.: The era-interim reanalysis: configuration and performance of the data assimilation system, Q. J. Roy. Meteorol. Soc., 137, 553–597, 2011.

deMenocal, P., Ortiz, J., Guilderson, T., Adkins, J., Sarnthein, M., Baker, L., and Yarusinsky, M.: Abrupt onset and termination of the African Humid Period: rapid climate responses to gradual insolation forcing, Quaternary Sci. Rev., 19, 347–361, 2000.

Drake, N., Candy, I., Breeze, P., Armitage, S., Gasmi, N., Schwenninger, J., Peat, D., and Manning, K.: Sedimen-

tary and geomorphic evidence of saharan megalakes: A synthesis, Quaternary Sci. Rev., 276, 107318, https://doi.org/10.1016/j.quascirev.2021.107318, 2022.

Egerer, S., Claussen, M., and Reick, C.: Rapid increase in simulated North Atlantic dust deposition due to fast change of northwest African landscape during the Holocene, Clim. Past, 14, 1051–1066, https://doi.org/10.5194/cp-14-1051-2018, 2018.

Guenther, A., Karl, T., Harley, P., Wiedinmyer, C., Palmer, P. I., and Geron, C.: Estimates of global terrestrial isoprene emissions using MEGAN (Model of Emissions of Gases and Aerosols from Nature), Atmos. Chem. Phys., 6, 3181–3210, https://doi.org/10.5194/acp-6-3181-2006, 2006.

Guenther, A. B., Jiang, X., Heald, C. L., Sakulyanontvittaya, T., Duhl, T., Emmons, L. K., and Wang, X.: The Model of Emissions of Gases and Aerosols from Nature version 2.1 (MEGAN2.1): an extended and updated framework for modeling biogenic emissions, Geosci. Model Dev., 5, 1471–1492, https://doi.org/10.5194/gmd-5-1471-2012, 2012.

Hantson, S., Knorr, W., Schurgers, G., Pugh, T. A., and Arneth, A.: Global isoprene and monoterpene emissions under changing climate, vegetation, CO_2 and land use, Atmos. Environ., 155, 35–45, 2017.

Heinold, B., Helmert, J., Hellmuth, O., Wolke, R., Ansmann, A., Marticorena, B., Laurent, B., and Tegen, I.: Regionalmodeling of Saharan dust events using LM-MUSCAT: Model description and case studies, J. Geophys. Res., 112, D11204, https://doi.org/10.1029/2006JD007443, 2007.

Hély, C., Lézine, A.-M., and contributors, A.: Holocene changes in African vegetation: tradeoff between climate and water availability, Clim. Past, 10, 681–686, https://doi.org/10.5194/cp-10-681-2014, 2014.

Huijnen, V., Williams, J., van Weele, M., van Noije, T., Krol, M., Dentener, F., Segers, A., Houweling, S., Peters, W., de Laat, J., Boersma, F., Bergamaschi, P., van Velthoven, P., Le Sager, P., Eskes, H., Alkemade, F., Scheele, R., Nédélec, P., and Pätz, H.-W.: The global chemistry transport model TM5: description and evaluation of the tropospheric chemistry version 3.0, Geosci. Model Dev., 3, 445–473, https://doi.org/10.5194/gmd-3-445-2010, 2010.

Jokinen, T., Berndt, T., Makkonen, R., Kerminen, V.-M., Junninen, H., Paasonen, P., Stratmann, F., Herrmann, H., Guenther, A. B., Worsnop, D. R., Kulmala, M., Ehn, M., and Sipilä, M.: Production of extremely low volatile organic compounds from biogenic emissions: Measured yields and atmospheric implications, P. Natl. Acad. Sci. USA, 112, 7123–7128, https://doi.org/10.1073/pnas.1423977112, 2015.

Joussaume, S., Taylor, K. E., Braconnot, P., Mitchell, J. F. B., Kutzbach, J. E., Harrison, S. P., Prentice, I. C., Broccoli, A. J., Abe-Ouchi, A., Bartlein, P. J., Bonfils, C., Dong, B., Guiot, J., Herterich, K., Hewitt, C. D., Jolly, D., Kim, J. W., Kislov, A., Kitoh, A., Loutre, M. F., Masson, V., McAvaney, B., McFarlane, N., de Noblet, N., Peltier, W. R., Peterschmitt, J. Y., Pollard, D., Rind, D., Royer, J. F., Schlesinger, M. E., Syktus, J., Thompson, S., Valdes, P., Vettoretti, G., Webb, R. S., and Wyputta, U.: Monsoon changes for 6000 years ago: Results of 18 simulations from the paleoclimate modeling intercomparison project (pmip), Geophys. Res. Lett., 26, 859–862, 1999.

Kaplan, J. O., Folberth, G., and Hauglustaine, D. A.: Role of methane and biogenic volatile organic compound sources in late glacial and holocene fluctuations of atmospheric methane concentrations, Global Biogeochem. Cy., 20, GB2016, https://doi.org/10.1029/2005GB002590, 2006.

Krinner, G., Lézine, A.-M., Braconnot, P., Sepulchre, P., Ramstein, G., Grenier, C., and Gouttevin, I.: A reassessment of lake and wetland feedbacks on the North African Holocene climate, Geophys. Res. Lett., 39, L07701, https://doi.org/10.1029/2012GL050992, 2012.

Krol, M., Houweling, S., Bregman, B., van den Broek, M., Segers, A., van Velthoven, P., Peters, W., Dentener, F., and Bergamaschi, P.: The two-way nested global chemistry-transport zoom model TM5: algorithm and applications, Atmos. Chem. Phys., 5, 417–432, https://doi.org/10.5194/acp-5-417-2005, 2005.

Kulmala, M., Suni, T., Lehtinen, K. E. J., Dal Maso, M., Boy, M., Reissell, A., Rannik, Ü., Aalto, P., Keronen, P., Hakola, H., Bäck, J., Hoffmann, T., Vesala, T., and Hari, P.: A new feedback mechanism linking forests, aerosols, and climate, Atmos. Chem. Phys., 4, 557–562, https://doi.org/10.5194/acp-4-557-2004, 2004.

Kulmala, M., Nieminen, T., Nikandrova, A., Lehtipalo, K., Manninen, H. E., Kajos, M. K., Kolari, P., Lauri, A., Petäjä, T., Krejci, R., Hansson, H.-C., Swietlicki, E., Lindroth, A., Christensen, T. R., Arneth, A., Hari, P., Bäck, J., Vesala, T., and Kerminen, V.-M.: CO_2-induced terrestrial climate feedback mechanism: From carbon sink to aerosol source and back, Boreal Environ. Res., 19, 122–131, 2014.

Kutzbach, J. E.: Monsoon climate of the early holocene: Climate experiment with the earth's orbital parameters for 9000 years ago, Science, 214, 59–61, 1981.

Leung, D. M., Kok, J. F., Li, L., Okin, G. S., Prigent, C., Klose, M., Pérez García-Pando, C., Menut, L., Mahowald, N. M., Lawrence, D. M., and Chamecki, M.: A new process-based and scale-aware desert dust emission scheme for global climate models – Part I: Description and evaluation against inverse modeling emissions, Atmos. Chem. Phys., 23, 6487–6523, https://doi.org/10.5194/acp-23-6487-2023, 2023.

Lézine, A.-M., Hély, C., Grenier, C., Braconnot, P., and Krinner, G.: Sahara and sahel vulnerability to climate changes, lessons from holocene hydrological data, Quaternary Sci. Rev., 30(, 3001–3012, 2011.

Lu, Z., Miller, P. A., Zhang, Q., Zhang, Q., Wårlind, D., Nieradzik, L., Sjolte, J., and Smith, B.: Dynamic vegetation simulations of the mid-holocene green sahara, Geophys. Res. Lett., 45, 8294–8303, 2018.

McGee, D., deMenocal, P. B., Winckler, G., Stuut, J. B. W., and Bradtmiller, L. I.: The magnitude, timing and abruptness of changes in north african dust deposition over the last 20,000 yr, Earth Planet. Sc. Lett., 371–372, 163–176, 2013.

Menviel, L., Govin, A., Avenas, A., Meissner, K. J., Grant, K. M., and Tzedakis, P. C.: Drivers of the evolution and amplitude of african humid periods, Commun. Earth Environ., 2, 237, https://doi.org/10.1038/s43247-021-00309-1, 2021.

Middleton, J. L., Mukhopadhyay, S., Langmuir, C. H., McManus, J. F., and Huybers, P. J.: Millennial-scale variations in dustiness recorded in Mid-Atlantic sediments from 0 to 70 ka, Earth Planet. Sc. Lett., 482, 12–22, 2018.

Myriokefalitakis, S., Daskalakis, N., Gkouvousis, A., Hilboll, A., Van Noije, T., Williams, J. E., Le Sager, P., Huijnen, V., Houweling, S., Bergman, T., Rasmus Nüß, J., Vrekoussis, M., Kanakidou, M., and Krol, M. C.: Description and evaluation of a detailed

gas-phase chemistry scheme in the TM5-MP global chemistry transport model (r112), Geosci. Model Dev., 13, 5507–5548, https://doi.org/10.5194/gmd-13-5507-2020, 2020.

Otto-Bliesner, B. L., Braconnot, P., Harrison, S. P., Lunt, D. J., Abe-Ouchi, A., Albani, S., Bartlein, P. J., Capron, E., Carlson, A. E., Dutton, A., Fischer, H., Goelzer, H., Govin, A., Haywood, A., Joos, F., LeGrande, A. N., Lipscomb, W. H., Lohmann, G., Mahowald, N., Nehrbass-Ahles, C., Pausata, F. S. R., Peterschmitt, J.-Y., Phipps, S. J., Renssen, H., and Zhang, Q.: The PMIP4 contribution to CMIP6 – Part 2: Two interglacials, scientific objective and experimental design for Holocene and Last Interglacial simulations, Geosci. Model Dev., 10, 3979–4003, https://doi.org/10.5194/gmd-10-3979-2017, 2017.

Pausata, F. S., Messori, G., and Zhang, Q.: Impacts of dust reduction on the northward expansion of the african monsoon during the green sahara period, Earth Planet. Sc. Lett., 434, 298–307, 2016.

Shrivastava, M., Cappa, C. D., Fan, J., Goldstein, A. H., Guenther, A. B., Jimenez, J. L., Kuang, C., Laskin, A., Martin, S. T., Ng, N. L., Petäjä, T., Pierce, J. R., Rasch, P. J., Roldin, P., Seinfeld, J. H., Shilling, J., Smith, J. N., Thornton, J. A., Volkamer, R., Wang, J., Worsnop, D. R., Zaveri, R. A., Zelenyuk, A., and Zhang, Q.: Recent advances in understanding secondary organic aerosol: Implications for global climate forcing, Rev. Geophys., 55, 509–559, 2017.

Sindelarova, K., Granier, C., Bouarar, I., Guenther, A., Tilmes, S., Stavrakou, T., Müller, J.-F., Kuhn, U., Stefani, P., and Knorr, W.: Global data set of biogenic VOC emissions calculated by the MEGAN model over the last 30 years, Atmos. Chem. Phys., 14, 9317–9341, https://doi.org/10.5194/acp-14-9317-2014, 2014.

Sindelarova, K., Markova, J., Simpson, D., Huszar, P., Karlicky, J., Darras, S., and Granier, C.: High-resolution biogenic global emission inventory for the time period 2000–2019 for air quality modelling, Earth Syst. Sci. Data, 14, 251–270, https://doi.org/10.5194/essd-14-251-2022, 2022.

Singarayer, J. S., Valdes, P. J., Friedlingstein, P., Nelson, S., and Beerling, D. J.: Late holocene methane rise caused by orbitally controlled increase in tropical sources, Nature, 470, 82–85, 2011.

Smith, B., Prentice, I. C., and Sykes, M. T.: Representation of vegetation dynamics in the modelling of terrestrial ecosystems: comparing two contrasting approaches within European climate space, Global Ecol. Biogeogr., 10, 621–637, 2001.

Smith, B., Wårlind, D., Arneth, A., Hickler, T., Leadley, P., Siltberg, J., and Zaehle, S.: Implications of incorporating N cycling and N limitations on primary production in an individual-based dynamic vegetation model, Biogeosciences, 11, 2027–2054, https://doi.org/10.5194/bg-11-2027-2014, 2014.

Specht, N. F., Claussen, M., and Kleinen, T.: Simulated range of mid-Holocene precipitation changes from extended lakes and wetlands over North Africa, Clim. Past, 18, 1035–1046, https://doi.org/10.5194/cp-18-1035-2022, 2022.

Tegen, I., Harrison, S. P., Kohfeld, K., Prentice, I. C., Coe, M., and Heimann, M.: Impact of vegetation and preferential source areas on global dust aerosol: Results from a model study, J. Geophys. Res.-Atmos., 107, AAC 14-1–AAC 14-27, 2002.

Thompson, A. J., Skinner, C. B., Poulsen, C. J., and Zhu, J.: Modulation of Mid-Holocene African Rainfall by Dust Aerosol Direct and Indirect Effects, Geophys. Res. Lett., 46, 3917–3926, 2019.

Tierney, J. E., Pausata, F. S., and De Menocal, P. B.: Rainfall regimes of the Green Sahara, Sci. Adv., 3, e1601503, https://doi.org/10.1126/sciadv.1601503, 2017.

van Marle, M. J. E., Kloster, S., Magi, B. I., Marlon, J. R., Daniau, A.-L., Field, R. D., Arneth, A., Forrest, M., Hantson, S., Kehrwald, N. M., Knorr, W., Lasslop, G., Li, F., Mangeon, S., Yue, C., Kaiser, J. W., and van der Werf, G. R.: Historic global biomass burning emissions for CMIP6 (BB4CMIP) based on merging satellite observations with proxies and fire models (1750–2015), Geosci. Model Dev., 10, 3329–3357, https://doi.org/10.5194/gmd-10-3329-2017, 2017.

van Noije, T., Bergman, T., Le Sager, P., O'Donnell, D., Makkonen, R., Gonçalves-Ageitos, M., Döscher, R., Fladrich, U., von Hardenberg, J., Keskinen, J.-P., Korhonen, H., Laakso, A., Myriokefalitakis, S., Ollinaho, P., Pérez García-Pando, C., Reerink, T., Schrödner, R., Wyser, K., and Yang, S.: EC-Earth3-AerChem: a global climate model with interactive aerosols and atmospheric chemistry participating in CMIP6, Geosci. Model Dev., 14, 5637–5668, https://doi.org/10.5194/gmd-14-5637-2021, 2021.

van Noije, T. P. C., Le Sager, P., Segers, A. J., van Velthoven, P. F. J., Krol, M. C., Hazeleger, W., Williams, A. G., and Chambers, S. D.: Simulation of tropospheric chemistry and aerosols with the climate model EC-Earth, Geosci. Model Dev., 7, 2435–2475, https://doi.org/10.5194/gmd-7-2435-2014, 2014.

Vignati, E., Wilson, J., and Stier, P.: M7: An efficient size-resolved aerosol microphysics module for large-scale aerosol transport models, J. Geophys. Res.-Atmos., 109, 1–17, 2004.

Williams, C. J. R., Guarino, M.-V., Capron, E., Malmierca-Vallet, I., Singarayer, J. S., Sime, L. C., Lunt, D. J., and Valdes, P. J.: CMIP6/PMIP4 simulations of the mid-Holocene and Last Interglacial using HadGEM3: comparison to the pre-industrial era, previous model versions and proxy data, Clim. Past, 16, 1429–1450, https://doi.org/10.5194/cp-16-1429-2020, 2020.

Williams, J. E., Boersma, K. F., Le Sager, P., and Verstraeten, W. W.: The high-resolution version of TM5-MP for optimized satellite retrievals: description and validation, Geosci. Model Dev., 10, 721–750, https://doi.org/10.5194/gmd-10-721-2017, 2017.

Williams, R. H., McGee, D., Kinsley, C. W., Ridley, D. A., Hu, S., Fedorov, A., Tal, I., Murray, R. W., and Demenocal, P. B.: Glacial to Holocene changes in trans-Atlantic Saharan dust transport and dust-climate feedbacks, Sci. Adv., 2, e1600445, Dhttps://doi.org/10.1126/sciadv.1600445, 2016.

Yarwood, G., Rao, S., Yocke, M., and Whitten, G. Z.: Updates to the Carbon Bond Chemical Mechanism: CB05, Final Report prepared for US EPA, Technical report, US EPA, ISBN 0009-2665, 2005.

Yli-Juuti, T., Mielonen, T., Heikkinen, L., Arola, A., Ehn, M., Isokääntä, S., Keskinen, H. M., Kulmala, M., Laakso, A., Lipponen, A., Luoma, K., Mikkonen, S., Nieminen, T., Paasonen, P., Petäjä, T., Romakkaniemi, S., Tonttila, J., Kokkola, H., and Virtanen, A.: Significance of the organic aerosol driven climate feedback in the boreal area, Nat. Commun., 12, 5637, https://doi.org/10.1038/s41467-021-25850-7, 2021.

Yukimoto, S., Koshiro, T., Kawai, H., Oshima, N., Yoshida, K., Urakawa, S., Tsujino, H., Deushi, M., Tanaka, T., Hosaka, M., Yoshimura, H., Shindo, E., Mizuta, R., Ishii, M., Obata, A., and Adachi, Y.: MRI MRI-ESM2.0 model output prepared for CMIP6 PMIP midHolocene, Version 20230611, Earth System

Grid Federation, https://doi.org/10.22033/ESGF/CMIP6.6860, 2019.

Zhang, Z., Bentsen, M., Oliviè, D. J. L., Seland, Ø., Toniazzo, T., Gjermundsen, A., Graff, L. S., Debernard, J. B., Gupta, A. K., He, Y., Kirkevåg, A., Schwinger, J., Tjiputra, J., Aas, K. S., Bethke, I., Fan, Y., Griesfeller, J., Grini, A., Guo, C., Ilicak, M., Karset, I. H. H., Landgren, O. A., Liakka, J., Moseid, K. O., Nummelin, A., Spensberger, C., Tang, H., Heinze, C., Iversen, T., and Schulz, M.: NCC NorESM2-LM model output prepared for CMIP6 PMIP midHolocene, Version 20230611, Earth System Grid Federation, https://doi.org/10.22033/ESGF/CMIP6.8079, 2019.

Zhou, P., Lu, Z., Keskinen, J.-P., Zhang, Q., Lento, J., Bian, J., van Noije, T., Le Sager, P., Kerminen, V.-M., Kulmala, M., Boy, M., and Makkonen, R.: Datasets for "Simulating the dust emissions and SOA formation over Northern Africa during the mid-Holocene Green Sahara period", Zenodo [data set], https://doi.org/10.5281/zenodo.8410150, 2023.